SBF
SOCIEDADE BRASILEIRA DE FÍSICA

PARTICLES AND FIELDS

The Dynamics of Apparent Horizons in Robinson–Trautman Spacetimes

**Henrique Pereira de Oliveira · Eduardo Lima Rodrigues ·
Ivano Damião Soares**

Abstract We present an alternative scheme of finding
apparent horizons based on spectral methods applied to
Robinson–Trautman spacetimes. We have considered
distinct initial data such as representing the spheroids
of matter and the head-on collision of two non-rotating
black holes. The evolution of the apparent horizon is
presented. We have obtained in some cases a mass gap
between the final Bondi and apparent horizon masses,
whose implications were briefly commented in the light
of the thermodynamics of black holes.

Keywords Apparent horizons · Robinson–Trautman
spacetimes · Spectral methods · Black holes

1 Introduction

One of the most important problems in classical general
relativity is the evolution of apparent horizons [1].
The apparent horizon [2] is defined as the outermost
marginally trapped surface that can be located on each
spacelike surface during the overall dynamics of the

H. P. de Oliveira (✉)
Departamento de Física Teórica, Instituto de Física,
Universidade do Estado do Rio de Janeiro,
20550-013 Rio de Janeiro, Rio de Janeiro, Brazil
e-mail: hp.deoliveira@pq.cnpq.br

E. L. Rodrigues · I. Damião Soares
Centro Brasileiro de Pesquisas Físicas/MCT, R. Dr. Xavier
Sigaud, 150, 22290-180 Rio de Janeiro, Rio de Janeiro, Brazil

E. L. Rodrigues
e-mail: eduardor@cbpf.br

I. Damião Soares
e-mail: ivano@cbpf.br

spacetime. According to cosmic censorship hypothesis,
there must exist outside the apparent horizon an event
horizon [2], and for this reason, apparent horizons are
the key structures that signalize the formation of black
holes in gravitational collapse, as well play relevant
role in the merging of black holes [3–5]. Besides the
apparent horizon, another typical structure present in
a spacetime that contains a black hole is the event hori-
zon, but its determination depends on the whole history
of the spacetime due to the fact that an event horizon is
the boundary that separates those null geodesics that
reach infinity from those that not. In essence, while
the event horizon is a global structure, the apparent
horizon is local meaning that it can be determined at
each instant. Therefore, the construction of apparent
horizon finders is a crucial issue in numerical relativ-
ity that has received a great deal of attention in the
last years [6]. Basically, these codes are built to solve
numerically the apparent horizon equation, which is a
nonlinear elliptical equation, simultaneously with the
numerical evolution of the spacetime.

In general, most of the numerical strategies to solve
the apparent horizon equation are based on the finite
difference techniques. On the other hand, numerical
codes based on spectral methods [7, 8] have increased
considerably in the last years mainly due to the econ-
omy of the computational resources to achieve a de-
sired accuracy. In this direction, we shall present here
a simple and efficient numerical strategy using a con-
venient combination of Galerkin [9] and collocation
methods [10, 11] to determine the evolution of the
apparent horizon of Robinson–Trautman (RT) space-
times [12, 13].

The RT spacetimes are the simplest class of asymp-
totically flat geometries admitting gravitational waves

with two interesting basic features: (a) A RT spacetime can be interpreted as describing the exterior geometry of a bounded or isolated system emitting gravitational waves; (b) for regular initial data, the RT spacetimes evolve asymptotically toward the Schwarzschild black hole [14–16]. For the sake of completeness, the line element of the Robinson–Trautman spacetimes can be conveniently written as

$$ds^2 = \left(\lambda(u, \theta) - \frac{2m_0}{r} + 2r\frac{\dot{K}}{K}\right) du^2 + 2du\,dr$$
$$- r^2 K^2(u, \theta)(d\theta^2 + \sin^2\theta\,d\varphi^2), \tag{1}$$

where u is a null coordinate such that $u = $ constant denotes null hypersurfaces generated by the rays of the gravitational field and that foliate the spacetime globally, r is an affine parameter defined along the null geodesics determined by the vector $\partial/\partial r$, and m_0 is a constant related to the Bondi mass. The overdot means derivative with respect to u. The Einstein equations can be cast in the following form:

$$\lambda(u, \theta) = \frac{1}{K^2} - \frac{K_{\theta\theta}}{K^3} + \frac{K_\theta^2}{K^4} - \frac{K_\theta}{K^3}\cot\theta \tag{2}$$

$$-6m_0\frac{\dot{K}}{K} + \frac{(\lambda_\theta\sin\theta)_\theta}{2K^2\sin\theta} = 0. \tag{3}$$

Here the subscript θ denote derivative with respect to the angle θ; the function $\lambda(u, \theta)$ is the Gaussian curvature of the surfaces ($u = $ const., $r = $ const.). The structure of the field equations is typical of a characteristic problem [17], in which the first equation is a hypersurface equation relating the functions $\lambda(u, \theta)$ and $K(u, \theta)$, whereas the second equation is the evolution equation. Accordingly, once the initial data $K(u_0, \theta)$ is prescribed on a given null surface $u = u_0$, the hypersurface equation fixes $\lambda(u_0, \theta)$, and the evolution equation determines $K(u, \theta)$ on the next null surface and the whole process repeats providing the evolution of the spacetime.

The only known analytical solution of the RT field equations is the Schwarzschild black hole described by,

$$K(\theta) = \frac{K_0}{\cosh\gamma + \cos\theta\sinh\gamma}. \tag{4}$$

This solution describes a boosted Schwarzschild black hole with constant $v = \tanh\gamma$ with respect to an inertial observer at infinity [18, 19]. The total mass energy of the boosted black hole is given by [20, 21] (see also (27)):

$$M_{BH} = \frac{m_0 K_0^3}{\sqrt{1 - v^2}}. \tag{5}$$

Notice the similarity of the above expression with the relativistic energy of a moving particle of rest mass $m_0 K_0^3$ and velocity v. The particular case of $\gamma = 0$ corresponds to a Schwarzschild black hole at rest.

This paper is divided as follows: In Section 2, we present the apparent horizon equation and the numerical strategy based on spectral methods adopted to solve it. In Section 3, we exhibit the numerical results that consists in testing the code along with the dynamics of the apparent horizon corresponding to initial data representing spheroids [22] and the collision of black holes [23] in RT spacetimes. Finally, the final remarks are presented in Section 4.

2 Solving the Apparent Horizon Equation Using Spectral Methods

As already mentioned, RT spacetimes have interesting features, such as the asymptotic flatness and the presence of gravitational waves, which can be interpreted as arising from a bounded distribution of matter evolving toward a Schwarzschild black hole and therefore indicating a simple example of non-spherical collapse. However, these geometries do not have a future apparent horizon characterized by the vanishing of the null expansion associated to outgoing future directed rays, but only past apparent horizon [24–26]. A past apparent horizon is the outermost boundary of past-trapped surfaces corresponding to that value of u; more precisely, consider a hypersurface S defined by $S = r - V(u, \theta) = 0$, and in particular, if S is a marginally past-trapped 2-surface, the ingoing normal null vector $n_\alpha = \partial_\alpha S$ has vanishing divergence

$$\theta_- = n^\alpha_{;\alpha} = 0. \tag{6}$$

From this equation, it can be shown [25] that the function $V(u, \theta)$ satisfies the following equation at each slice $u = $ constant:

$$\frac{1}{\sin\theta}\left(\sin\theta\frac{V_\theta}{V}\right)_\theta - \lambda K^2 + \frac{2m_0}{V}K^2 = 0, \tag{7}$$

which is known as the apparent horizon equation. The dynamics of the apparent horizon is obtained after solving this equation at each hypersurface $u = $ constant, where the function $K(u, \theta)$ is determined from the evolution (3). There are few analytical results about the properties of past apparent horizons in RT spacetimes. Tod [25] has shown the validity of the isoperimetric inequality and the existence of a unique marginally past-trapped surface at each hypersurface $u = $ constant.

The apparent horizon equation (7) will be solved here using a numerical scheme based on a suitable

combination of Galerkin and collocation methods in a similar way we have implemented to solve the field equations (2) and (3). For this reason, we shall briefly outline our previous numerical scheme [27, 28] for solving the field equations and, in the sequence, the procedure employed to integrate the apparent horizon equation.

According to [28], the first step is to establish the Galerkin expansion for the function $K(u, \theta)$,

$$K_a^2(u, x) = e^{Q_a(u,x)} = \exp\left(\sum_{k=0}^{N} b_k(u) P_k(x)\right),$$ (8)

where the subscript a indicates an approximation of the exact $K(u, x)$. The angular coordinate θ is replaced by $x = \cos\theta$, N is the truncation order that indicates where the series stops, and the $N + 1$ modes $b_k(u)$ are unknown functions of u to be determined; the Legendre polynomials $P_k(x)$ were chosen as the basis or the trial functions. Next, an approximate expression for the function $\lambda(u, x)$ is obtained after substituting the above expansion into the constraint equation (2), or

$$\lambda_a(u, x) = e^{-Q_a(u,x)}\left(1 + \sum_{k=0}^{N} \frac{k(k+1)}{2} b_k(u) P_k(x)\right).$$ (9)

These last two equations are substituted into (3) to yield what is known as the residual equation associated to the evolution equation,

$$\text{Res}_K(u, x) = 6 m_0 \sum_{k=0}^{N} \dot{b}_k(u) P_k(x)$$
$$- e^{-Q_a(u,x)}\left[\left(1 - x^2\right) \lambda_a'\right]',$$ (10)

where prime denotes derivative with respect to x. Notice that the residual equation does not vanish exactly due to the adopted approximations for the functions $K(u, x)$ and $\lambda(u, x)$, but as we have shown, it converges to zero as the truncation order N is increased [28]. Following the Galerkin method, the projections of the residual equation with respect to a suitable set of test functions $\Psi_n(x)$ vanish, namely

$$\langle\text{Res}_K(u, x), \Psi_n(x)\rangle = \int_{-1}^{1} \text{Res}_K(u, x)\Psi_n(x)\, dx = 0,$$ (11)

for $n = 0, 1, ..N$. It means that the modes $b_j(u)$ are chosen in such a way that the residual equation is forced to be zero in an average sense [29]. Following the Galerkin method, we have selected, for the above integrations, the test functions to be same as the trial functions, $\Psi_n(x) = P_n(x)$. At this point, we have intro-

duced an additional approximation for the exponential term given by

$$\exp(-Q_a(u, x)) \approx \sum_{j=0}^{\bar{N}} c_j T_j(x),$$ (12)

where $T_j(x)$ is the Chebyshev polynomial of order j and $\bar{N}$ indicates the number of modes c_j. Basically, the motivation behind this approximation is to allow rapid and direct integrations of the residual equation. As a consequence of the above expansion, the $\bar{N} + 1$ modes c_j are related to the $N + 1$ modes b_k by assuming that the projections of the residual equation $\text{Res}_Q(u, x) = \exp(-Q_a(u, x)) - \sum_{j=0}^{\bar{N}} c_j T_j(x)$ with respect to the test functions $\Psi_n(x) = \delta(x - x_n)$ vanish, where $x_n = \cos(\pi n/\bar{N})$ are the Chebyshev–Gauss–Lobatto collocation points. The additional approximation (12) is introduced into (11), and after performing the $N + 1$ integrals, a set of ordinary differential equations for the modes $b_k(u)$ arises. Therefore, evolving these equations is equivalent to determining the dynamics of RT spacetimes, since the function $K(u, x)$ can be reconstructed at each u.

The past horizon equation (7) will be solved at each time level u by applying a similar combination of spectral methods as described previously. We have followed [25] and introduced an auxiliary function $F(u, x)$ by setting

$$V = 2m_0 \exp(-F),$$ (13)

in order to eliminate m_0 from the apparent horizon equation. A natural Galerkin expansion for $F(u, x)$ is given by

$$F_a(u, x) = \sum_{k=0}^{M} a_k(u) P_k(x),$$ (14)

where M is the truncation order not necessarily the same as N (see (8)). The apparent horizon equation is rewritten in function of $F(u, x)$, and after substituting the above expansion together with the approximate expressions for $K(u, x)$ and $\lambda(u, x)$ ((8) and (9)), we have obtained the residual equation associated to the apparent horizon equation

$$\text{Res}_{AH}(u, x) = \left[\left(1 - x^2\right) F_a'\right]' + 1 + \sum_{k=0}^{N} \frac{1}{2}k(k+1)$$
$$\times b_k(u) P_k(x) - \exp(F_a + Q_a).$$ (15)

As we have described before, the next step is to impose that all projections of the residual equation

(15) with respect to each basis function, $P_n(x)$, $n = 0, 1, ..., M$, must vanish. Schematically, we have

$$\langle \text{Res}_{\text{AH}}, P_n(x) \rangle = \int_{-1}^{1} \text{Res}_{\text{AH}}(u, x) P_n(x) = 0. \quad (16)$$

Notice the presence of two exponential terms in the residual equation (15) that can be reexpressed using additional approximations as,

$$\exp(F_{\text{a}}(u, x)) \approx \sum_{k=0}^{\bar{M}} \alpha_k T_k(x), \quad (17)$$

$$\exp(Q_{\text{a}}(u, x)) \approx \sum_{k=0}^{\bar{M}} \beta_k T_k(x), \quad (18)$$

where α_k and β_k are the modes associated to these new approximations and $\bar{M}$ is the truncation order for both expansions. The projections of the corresponding residual equations, $\text{Res}_F = \exp(F_{\text{a}}(u, x)) - \sum_{k=0}^{\bar{M}} \alpha_k T_k(x)$ and $\text{Res}_Q = \exp(Q_{\text{a}}(u, x)) - \sum_{k=0}^{\bar{M}} \beta_k T_k(x)$, with respect to the test functions $\delta(x - x_n)$, with $x_n = \cos(\pi n / \bar{M})$, are forced to vanish. Consequently, two sets of $\bar{M} + 1$ algebraic equations relating the modes (α_k, β_k) with (a_j, b_k), respectively, are generated. These approximate expressions are then inserted into (16), yielding

$$\langle \text{Res}_{\text{AH}}, P_n(x) \rangle$$

$$= \int_{-1}^{1} \left\{ \left[\left(1 - x^2 \right) F_a' \right]' + 1 + \frac{1}{2} \right.$$

$$\times \sum_{k=0}^{N} k(k+1) b_k(u) P_k(x)$$

$$\left. - \sum_{k,j=0}^{\bar{M}} \alpha_k(u) \beta_j(u) T_k(x) \times T_j(x) \right\} P_n(x) = 0. \quad (19)$$

After performing the above integrals, a set of $M + 1$ algebraic equations of the type $f_k(a_j, b_j, \alpha_i, \beta_i) = 0$ is obtained. Since we can express the modes α_k and β_k in terms of a_j and b_j and the modes b_k are known at each u, we can solve, in principle, this set of algebraic equations for the modes a_k and therefore determining the apparent horizon as described by (14).

3 Numerical Results

In this section, we present the numerical tests of our code as well the results about the dynamics of apparent horizons in RT spacetimes. We first need to specify the

initial data $K(u = 0, x)$ that determine the initial values for the $N + 1$ modes $b_k(0)$ through

$$b_j(0) = \frac{2 \langle \ln K(0, x), P_j \rangle}{\langle P_j, P_j \rangle}. \quad (20)$$

We are going to consider two initial data in our numerical experiments. The first represents the exterior spacetime of a homogeneous oblate spheroid described by [22]

$$K(0, x) = \left[1 + \frac{B_0}{2} \left(\alpha(\zeta_0) + \frac{1}{2} \beta(\zeta_0) P_2(x) \right) \right]^2, \quad (21)$$

where ζ_0 and B_0 are free parameters and $\alpha(\zeta_0) = \arctan(1/\zeta_0)$, $\beta(\zeta_0) = (1 + 3\zeta_0^2) \arctan(1/\zeta_0) - 3\zeta_0$. There is a clear astrophysical motivation for such a family of initial data as pointed out in the works on the axisymmetric gravitational collapse of oblate gas spheroids satisfying the Vlasov equation either in Newtonian theory [30], as well in its relativistic generalization [31, 32], and also connected with the efficiency of the emission of gravitational waves [33]. The second initial data family describes two initially boosted Schwarzschild black holes with opposite velocities $v = \tanh \eta_0$ [23] in which

$$K(0, x) = \left(\frac{A_1}{\sqrt{\cosh \eta_0 - x \sinh \eta_0}} \right.$$

$$\left. + \frac{A_2}{\sqrt{\cosh \eta_0 + x \sinh \eta_0}} \right)^2, \quad (22)$$

where A_1 and A_2 are arbitrary positive constants associated to the mass of each black hole.

We first exhibit an important test for the spectral code used to integrate numerically the field equations (2) and (3). In spite of non-stationary analytical solutions of the field equations are not known (unless in the linear regime), there exists a conserved quantity

$$I_0 = \int_{-1}^{1} K^2(u, x) \mathrm{d}x, \quad (23)$$

which is derived from the field equations and interpreted as the area of the 2-sphere spanned by (θ, ϕ). The conservation of I_0 can be deduced after multiplying (3) by K^2 and integrating in the angular domain. Then, by specifying the initial data $K(0, x)$, the initial value of I_0 will be fixed and must be kept constant until the asymptotic state is achieved. In order to test if the numerically generated solution is accurate, we have evaluated the relative error between the numerical and exact values of I_0, $\sigma = |I_0 - I_{\text{numer}}| / I_0$, whose result is shown in Fig. 1 where we have included the influence of increasing truncation orders, or $N = 7, 9, 13$ (cf. (8)). As it can be observed, the conservation of I_0 is attained to about $10^{-8} \%$ accuracy for the smallest truncation
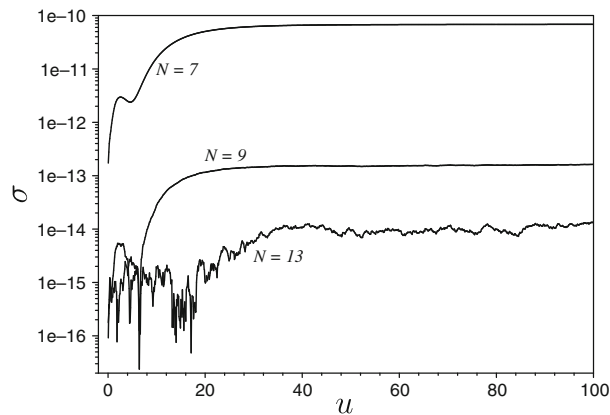
Fig. 1 Evolution of the relative error σ between I_0 and I_{numer}. We have considered the initial data that represent two initially boosted Schwarzschild black holes (22) with $A_1 = 1.0$, $A_2 = 0.2$, and $\eta_0 = 0.3$, as well distinct truncation orders $N = 7, 9, 13$ associated to the Galerkin expansion of $K(u, x)$ given by (8)

order $N = 7$ and about 10^{-12}% accuracy for $N = 13$. Therefore, this result is a vivid proof of the accuracy of the numerical evolution scheme despite those other tests described in [28].

We now proceed with the numerical tests of the algorithm used to solve the apparent horizon equation (7) at each time level u. Two steps will be needed. The first is to evaluate the time evolution of all modes $b_k(u)$ by integrating the dynamical system resulting from (11). In the second step, these modes calculated at each u are inserted into the system of $M + 1$ algebraic equations derived from (19) and solve them to obtain the corresponding modes $a_k(u)$ that describe the apparent horizon through the function $V(u, x)$ (cf. (13) and (14)). In this way, the evolution of the apparent horizon is obtained until the stationary solution is attained. As a matter of fact, as an important piece of evidence of the accuracy of our numerical scheme, we have plotted in Fig. 2 the modulus of the residual equation (15) evaluated at the initial instant $u = 0$ for both initial data families (21) and (22) taking into account distinct values of the truncation orders N and M associated to the functions $K(u, x)$ and $V(u, x)$ (cf. (8) and (14)). According to these plots, the residual equation approaches to zero as a consequence of increasing the truncation orders under consideration.

A more enlightening experiment for depicting the convergence of the code is to exhibit the evolution of the L_2 norm corresponding to the residual equation (15) given by

$$L_2 = \sqrt{\frac{1}{2} \int_{-1}^{1} \mathrm{Res}_{AH}(u, x)^2 \mathrm{d}x}, \qquad (24)$$
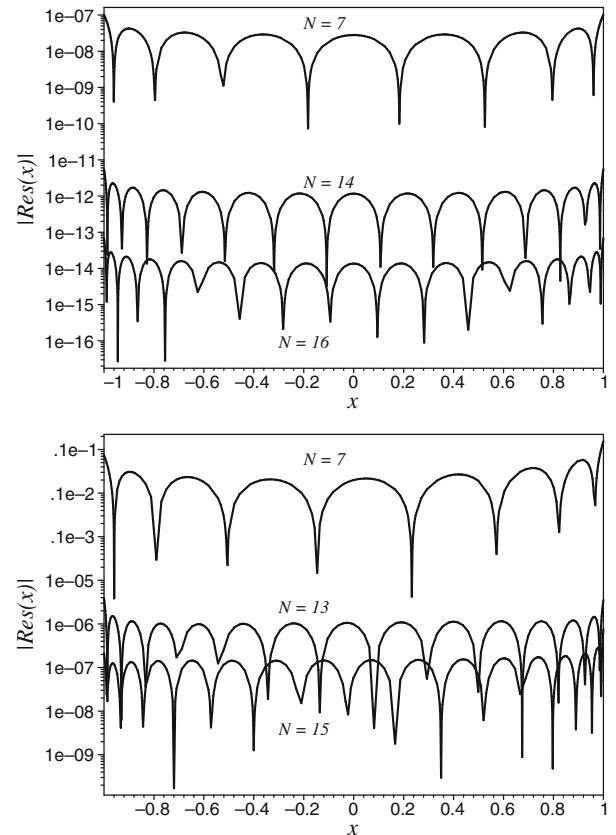

Fig. 2 Log-linear plots of the residual equation associated to the apparent horizon equation (15) showing the effect of increasing the truncation orders N as indicated above and $M = N$ in each case. Notice the decrease of the residual equation as more terms are included in the Galerkin expansion. The initial data are the oblate spheroid given by (21) with $\zeta_0 = 0.1$ and $B_0 = 1$ (*first graph*) and the two initially boosted black holes (22) in which $A_1 = 1.0$, $A_2 = 0.1$, and $\eta_0 = 0.3$

considering again distinct values of the truncation orders N and M. The convergence of the code is shown in Fig. 3 with the above norm evaluated at $u = 0.4$ for increasing values of N. Note the exponential decay of the error until the saturation due to round-off error is achieved for $N = 29$. In Fig. 4, we present the full evolution of L_2 is presented for distinct truncation orders M, N as an illustration of the rapid decrease of the error.

The evolution of the apparent horizon is illustrated by a sequence of polar plots of $r = V(u, x)$ and depicted in Fig. 5. We started at $u = 0$ with the oblate spheroid initial data (21), and several plots are shown in subsequent instants until $u_f = 500$ where a circle is formed. Indeed, this is a consequence from the fact that the asymptotic state is the Schwarzschild configuration
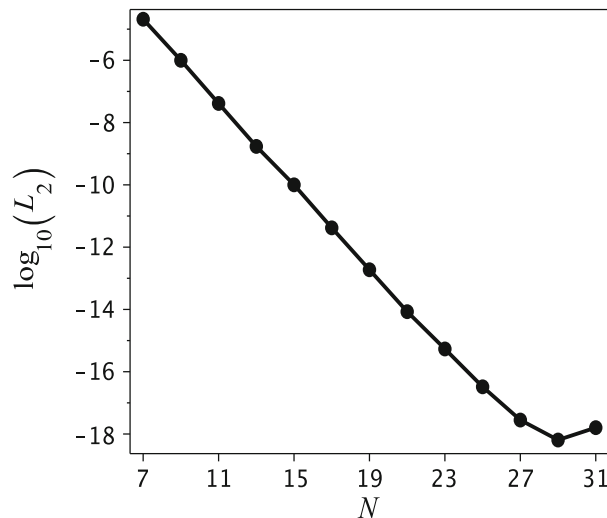
Fig. 3 The L_2 norm of the residual equation (24) evaluated at $u = 0.4$ and for several truncation orders. Notice the typical exponential decay of the norm with the increase of the truncation order until the saturation due to round-off error is achieved. Here we have used the two boosted black holes (22) with $A_1 = 1.0$, $A_2 = 0.15$, and $\eta_0 = 0.4$ as the initial data

characterized by $K = $ constant according to (7) which implies also in $V = $ constant.

An interesting application of our code is to follow the behavior of the apparent horizon mass that is basically the amount of mass enclosed by the apparent horizon. It is worth of mentioning that the apparent horizon mass has thermodynamical properties similar to those
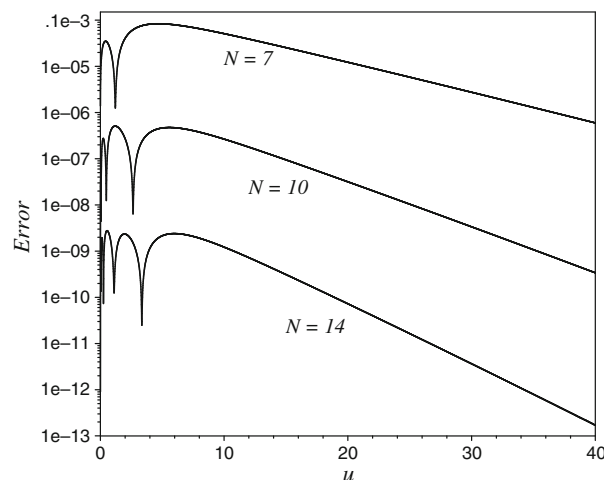

Fig. 4 Behavior of the L_2 norm of the apparent horizon equation (cf. (24)) for the oblate spheroid (21) with $\zeta_0 = 0.1$ and $B_0 = 0.3$ taking into account distinct truncation orders N and with $M = N$ in each case. Again as far as N is increased, more rapidly the norm tend to zero
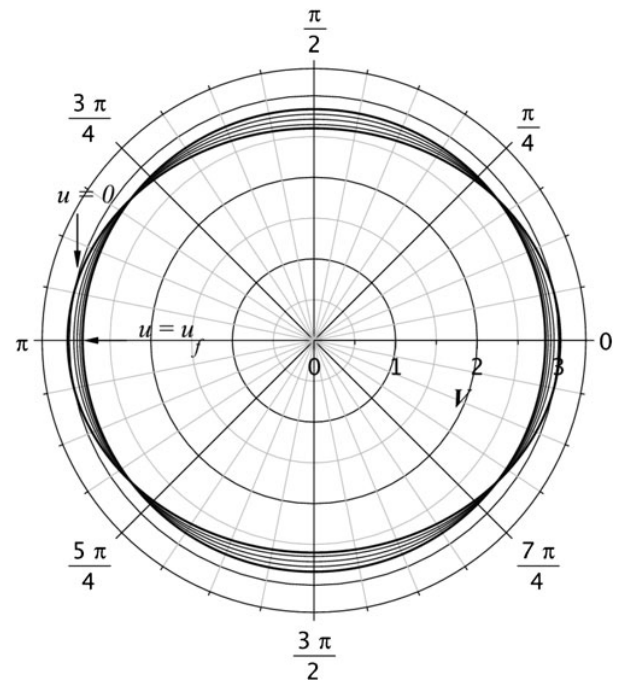

Fig. 5 Dynamics of all modes $a_k(u)$ through a sequence of polar plots of $2m_0 \exp(-F_a(u, x))$ starting from the oblate spheroid initial data ($\zeta_0 = 0.1$ and $B_0 = 0.4$) at $u_0 = 0$ as indicated and for several times until the Schwarzschild final configuration (represented by a *circle*) is formed at approximately $u_f = 500$

associated to black holes [26]. In the case of RT spacetimes, the past apparent horizon can only decrease in area, and therefore, its mass decreases, contrary to the monotonic increase of the future apparent horizon area. The apparent horizon area S_{AH} is evaluated through the following expression:

$$S_{AH} = 2\pi \int_{-1}^{1} r^2 K^2(u, x) dx$$

$$= 8\pi m_0^2 \int_{-1}^{1} e^{-2F(u,x)} K^2(u, x) dx, \qquad (25)$$

where $r = V(u, x) = 2m_0 e^{-2F(u,x)}$ describes the apparent horizon (cf. (13)) and the apparent horizon mass is expressed as

$$M_{AH} = \sqrt{\frac{S_{AH}}{16\pi}}. \qquad (26)$$

In Fig. 6, we present the evolution of the apparent horizon mass and the Bondi mass [20, 21]

$$M_B = \frac{1}{2} m_0 \int_{-1}^{1} K^3(u, x) dx, \qquad (27)$$

for the first family of initial data (21). According to [22], the asymptotic configuration is the Schwarzschild black hole whose final mass assumes the value $M_{\mathrm{BH}} = m_0 K_0^3$, where $K_0 = \lim_{u \to \infty} K(u, x)$. This amount is smaller than the mass associated to the initial data since part of it is extracted by gravitational waves [18, 19] during the evolution of the spacetime and consequently producing a monotonic decrease of the Bondi mass as shown in Fig. 6. Nonetheless, the decay of the apparent horizon mass is due to the decrease in area of the past apparent horizon as we have mentioned before. Notice also that both final values of the apparent horizon and Bondi masses coincide. As a matter of fact, this result is expected from the asymptotic solution of the apparent horizon equation $V_{\mathrm{asympt}} = 2m_0 K_0^2$, and together with the expression for the apparent horizon mass (26), one can arrive at $M_{\mathrm{AH}} = M_{\mathrm{BH}} = m_0 K_0^3$.

The final task is to consider the second family of initial data (22) which represent the head-on collision of two Schwarzschild black holes and a generalization of the initial data (21) that describe the exterior of an inhomogeneous oblate spheroid [22]. The common feature of both initial data is that the asymptotic configuration will be a boosted black hole [22, 23] described by

$$\lim_{u \to \infty} K(u, x) = \frac{\bar{K}_0}{\cosh \mu + x \sinh \mu}, \qquad (28)$$

where the values of $\bar{K}_0$ and the boost parameter μ are fixed by the numerical solution of the RT equation (see [23] for details) and the final Bondi mass is given

by (5). It is worth mentioning that the imbalance in momentum of the initial gravitational wave distribution is responsible for the boost of the resulting black hole. In Fig. 7, we observe again the monotonic decay of both M_{AH} and M_{B} with the retarded time u, but there is a gap between their asymptotic values. In order to understand the origin of this gap, we have noticed that according to the numerical experiments, the asymptotic
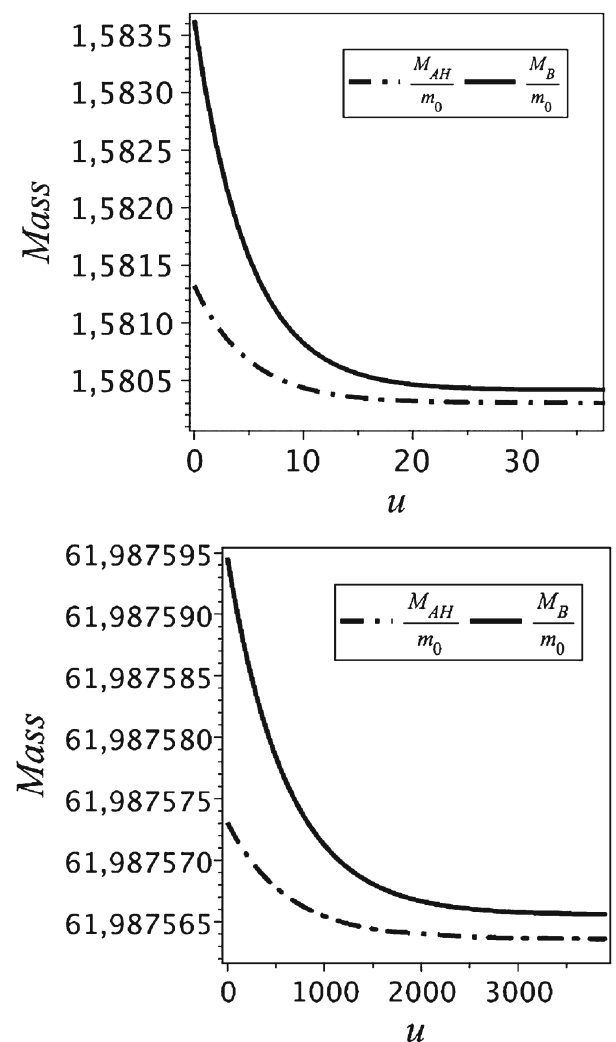
Fig. 7 Numerical decays of Bondi and apparent horizon masses in units of m_0. Here the final configuration is a boosted black hole, and both values of mass do not coincide asymptotically. The Bondi mass given by (5) gather the rest and kinetic energy of the hole, whereas the apparent horizon mass M_{AH} is a measure of the rest mass. We have considered in the first panel a nonhomogeneous oblate spheroid initial data [22] given by $K(0, x) = \left[1 + 0.05\left(\alpha(\zeta_0) + \frac{1}{2}\beta(\zeta_0) P_2(x)\right) + 0.05 \exp(x - 0.3)^2\right]^2$, $\zeta_0 = 0.1$, whereas in the second panel the head-on collision of two boosted black holes with $\eta_0 = 0.05$, $A_1 = 1.0$ and $A_2 = 0.99$
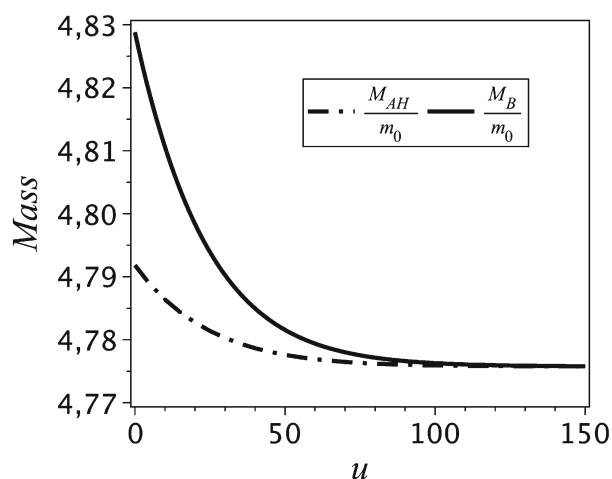

Fig. 6 Numerical evolution of the Bondi and apparent horizon masses in units of m_0 attesting their monotonic decay until the final configuration identified as the Schwarzschild black hole in which both values coincides. The initial data are the oblate spheroid with $\zeta_0 = 0.1$ and $B_0 = 0.4$.

solution of the apparent horizon equation (7) is the same as the previous case, $V_{\text{asympt}} = 2m_0 \bar{K}_0{}^2$, in spite of K_{asympt} not being a constant (cf. (27)). Therefore, the final value of the apparent horizon mass can be evaluated from (26) (note that in this situation $K = K(x)$) and whose result is $M_{\text{AH}} = m_0 \bar{K}_0{}^3$. In fact, this value is exactly the rest mass of the boosted black hole, and consequently, the gap observed in both graphs of Fig. 7 is due to the kinetic energy of the resulting black hole.

The above results can be interpreted in the light of the so-called first law of black hole thermodynamics [34, 35]. The final mass configurations displayed in each of Fig. 7 can actually be interpreted as two static black holes boosted with respect to the each other, namely they are connected by a K-transformation of the BMS group [18, 19] corresponding to a boost along the z-axis, as given by (28). This is the origin of the gap in Fig. 7, which has the value $M_{\text{B}}/M_{\text{AH}} = \cosh\mu$, where μ is the boost parameter of the K-transformation specified in (28). Now the entropy of each final black hole, considered as a thermodynamical system in equilibrium, is defined as proportional to the area $\mathcal{A}$ of its event horizon and is invariant by a K-transformation as can be easily verified. This should be expected since an eventual possible definition of the BH entropy by a counting of its microscopic states could not depend, in principle, on the state of motion of stationary black holes relative to inertial frames at infinity. Therefore, we have $\delta(\mathcal{A}/4\pi G) = \delta M_{\text{B}}/T_{\text{B}} = \delta M_{\text{AH}}/T_{\text{AH}}$ so that this gap also defines the temperature transformation $T_{\text{B}} \to T_{\text{B}} \cosh\mu$ between the two inertial rest frames of the BHs.

4 Final Considerations

In this paper, we have implemented and tested a numerical scheme based on a combination of Galerkin and pseudo-spectral methods to solve the apparent horizon equation in RT spacetimes. This a direct extension of the previous algorithm [28] used to integrate the field equations (2) and (3). The apparent horizon equation is reduced to a set of nonlinear algebraic equations for the modes a_k and whose solution at each instant determines the apparent horizon described by (7). The applications have consisted in solving the apparent horizon corresponding to initial data describing the exterior fields of oblate spheroids and the collision of two Schwarzschild black holes.

We have performed numerical tests that strongly indicate the convergence and accuracy of the code. In our numerical experiments, two initial data families in RT spacetimes were considered: The first represents the gravitational field outside a oblate spheroid while the second two initially boosted Schwarzschild black holes with opposed velocities. We have confirmed that the Bondi mass M_{B} decreases monotonically as the result of the mass extraction due to the gravitational waves, until a asymptotic value that coincides with the total mass of the resulting Schwarzschild black hole. The apparent horizon mass M_{AH} also decreases with respect to u in face of the decreased in area which is expected in the case of past apparent horizon. By considering the first initial data, the asymptotic values of M_{B} and M_{AH} coincide to the value of the total mass of the resulting Schwarzschild black hole. In this case, the apparent horizon mass is exactly the mass enclosed by the event horizon. On the other hand, if we take into account the second initial data, a gap between the asymptotic values of both masses is observed similarly as noticed by Chow and Lun [26]. The origin of the gap is associated to the final configuration identified as a boosted Schwarzschild black hole for which the Bondi mass is the total mass energy content that includes the rest mass $m_0 \bar{K}_0^3$ plus the kinetic energy, whereas the final apparent horizon mass is the rest mass.

Finally, in spite of RT spacetimes being the simplest asymptotically flat radiating geometries, they can be potentially used as simple but useful theoretical laboratories to study relevant features of the bounded sources emitting gravitational waves (see [22, 23, 27, 36]) and also to test new numerical schemes such as the one we have implemented here. The natural step in our research is to examine the evolution of apparent horizons in the case of general RT spacetimes and also in more realistic frameworks such as for spacetimes with Brill waves.

References

1. A. Ashtekar, B. Krishnan, Isolated and dynamical horizons and their applications. Living Rev. Relat. **7**, 10 (2004), http://www.livingreviews.org/lrr-2004-10
2. S.W. Hawking, G.F.R. Ellis, *The Large Scale Structure of Spacetime* (Cambridge University Press, Cambridge, 1973)
3. F. Pretorius, Phys. Rev. Lett. **95**, 121101 (2005)
4. M. Campanelli, C.O. Lousto, P. Marronetti, Y. Zlochower, Phys. Rev. Lett. **96**, 111101 (2006)
5. J.G. Baker, J. Centrella, D. Choi, M. Koppitz, J. van Meter, Phys. Rev. Lett. **96**, 111102 (2006)

6. J. Thornburg, Event and apparent horizon finders for $3 + 1$ numerical relativity. Living Rev. Relat. **10**, 3 (2007), http://www.livingreviews.org/lrr-2007-3
7. S. Bonazzola, E. Gourgoulhon, J.A. Marck, J. Comput. Appl. Math. **109**, 433 (1999)
8. P. Grandclément, J. Novak, Spectral methods for numerical relativity. Living Rev. Relat. **12**, 1 (2009), http://www.livingreviews.org/lrr-2009-1
9. P. Holmes., John L. Lumley, Gal Berkooz, *Turbulence, Coherent Structures, Dynamical Systems and Symmetry* (Cambridge University Press, Cambridge, 1998)
10. J.P. Boyd, *Chebyshev and Fourier Spectral Methods* (Dover, Mineola, 2001)
11. C. Canuto, M.Y. Hussaini, A. Quarteroni, T.A. Zang, *Spectral Methods, Fundamentals in Single Domains* (Springer, Berlin, 2006)
12. I. Robinson, A. Trautman, Phys. Rev. Lett. **4**, 431 (1960)
13. I. Robinson, A. Trautman, Proc. Roy. Soc. A **265**, 463 (1962)
14. P. Chrusciel, Commun. Math. Phys. **137**, 289 (1991)
15. P. Chrusciel, Proc. R. Soc. Lond. **436**, 299 (1992)
16. P. Chrusciel, D.B. Singleton, Commun. Math. Phys. **147**, 137 (1992)
17. Jeffrey Winicour, Characteristic evolution and matching, Living Rev. Relat. **8**, 10 (2005), http://www.livingreviews.org/lrr-2005-10
18. H. Bondi, M.G.J. van der Berg, A.W.K. Metzner, Proc. R. Soc. Lond., A **269**, 21 (1962)
19. R.K. Sachs, Phys. Rev. **128**, 2851 (1962)
20. U. von der Gönna, D. Kramer, Class. Quant. Grav. **15**, 215 (1998)
21. H.P. de Oliveira, I. Damião Soares, Phys. Rev. D **71**, 124034 (2005)
22. H.P. de Oliveira, E.L. Rodrigues, Class. Quantum Gravity **25**, 205020 (2008)
23. R. Aranha, H.P. de Oliveira, I.D. Soares, E.V. Tonini, Int. J. Mod. Phys. D **17**, 1 (2008)
24. R. Penrose, Ann. N.Y. Acad. Sci. **224**, 115 (1973)
25. K.P. Tod, Class. Quantum Gravity **6**, 1159 (1989)
26. E.W. Chow, A.W. Lun, J. Aust. Math. Soc. B **41**, 217 (1995)
27. H.P. de Oliveira, I. Damião Soares, Phys. Rev. D **70**, 084041 (2004)
28. H.P. de Oliveira, E.L. Rodrigues, I. Damião Soares, E.V. Tonini, Int. J. Mod. Phys. C **18**, 1853 (2007)
29. B.A. Finlayson, *The Method of Weighted Residuals and Variational Principles* (Academic, New York, 1972)
30. C.C. Lin, L. Mestel, F.H. Shu, Astrophys. J. **142**, 1431 (1965)
31. S.L. Shapiro, S.L. Teukolsky, Phys. Rev. Lett. **66**, 994 (1991)
32. S.L. Shapiro, S.L. Teukolsky, Phys. Rev. D **45**, 2006 (1992)
33. D.M. Eardley, Phys. Rev. D **12**, 3072 (1975)
34. J.D. Bekenstein, Phys. Rev. D **7**, 2333 (1973)
35. R.M. Wald, *General Relativity* (University of Chicago Press, Chicago, 1984)
36. H.P. de Oliveira, I. Damião Soares, E.V. Tonini, Phys. Rev. D **78**, 044017 (2008)